Sensors and Materials, Vol. 38, No. 6 (2026) 3051–3068
MYU Tokyo

S & M 4488

Plane-stress Needle-probe Measurement System for Characterizing the Inverse Magnetostrictive Behavior of Electrical Steel Under Tensile and Compressive Deformations

Guan-Ming Chen,[1] Wei-Hao Chang,[1] Kai-Fan Lo,[1] and Shih-Kang Kuo[2*]

[1]Green Energy & System Integration Research & Development Department, China Steel Corporation, Kaohsiung 81233, Taiwan
[2]Department of Mechanical Engineering, National Kaohsiung University of Science and Technology, Kaohsiung 80778, Taiwan

(Received February 17, 2026; accepted May 13, 2026)

Keywords: electrical steel, residual stress, magnetostrictive effect, motor

The electrical steel used in motor cores frequently experiences magnetic property degradation owing to elastic deformation and residual stress introduced during manufacturing processes. The quantitative characterization of the inverse magnetostrictive behavior, however, remains challenging because conventional measurement approaches typically require bulky loading systems and laminated specimens. We present a compact measurement system for characterizing the inverse magnetostrictive behavior of an electrical steel sheet using a plane-stress needle-probe method. By applying the plane-stress elasticity principle, compressive strain can be generated through Poisson's effect during tensile loading, enabling both tensile and equivalent compressive magnetic characterizations using a single-sheet specimen. A dual-core excitation structure is employed to ensure symmetric magnetic flux distribution across the sheet thickness, while the calibration based on Epstein-frame reference data provides quantitative consistency with standard magnetic measurements. Experimental evaluation on a 0.5-mm-thick non–grain-oriented electrical steel sheet demonstrates that compressive deformation causes a significantly greater magnetic degradation than tensile deformation, particularly in the low-flux permeability region. Comparative measurements on materials with different iron-loss grades further reveal variations in stress sensitivity that are relevant to motor design. The proposed measurement system provides a compact and practical platform for investigating stress-induced magnetic degradation in electrical steel and offers useful reference data for motor design and material development.

1. Introduction

Electrical steel (ES) exhibits a well-known magnetostriction phenomenon, in which its magnetic state and elastic deformation mutually affect each other. This phenomenon is commonly found in ferromagnetic materials and primarily originates from the coupling effect

*Corresponding author: e-mail: kuo67@nkust.edu.tw
https://doi.org/10.18494/SAM6297

ISSN 0914-4935
https://myukk.org/

between electron spin states and orbital motion, known as spin-orbit coupling.(1) The magnetostrictive effect is further explained in Fig. 1. The magnetic field applied to a ferromagnetic material changes the direction of electron spin, and through coupling, alters the orbital shape, thereby modifying the macroscopic dimensions of the material. This phenomenon is reversible. The material deformation caused by externally applied stress can alter magnetic properties, a phenomenon also known as inverse magnetostriction. In the motor industry, electromagnetic steel undergoes significant deformations during manufacturing. This makes the inverse magnetostriction effect highly relevant, as even small applied forces can directly affect the material's magnetic properties and overall performance. Only a few studies have been conducted to investigate the magnetic degradation caused by deformations. For example, measurement techniques have been developed to quantify the increased iron loss and reduced magnetic flux density in punched ES sheets.(2–5) Our previous study results on the punched edge are shown in Fig. 2. Both the simulation [Fig. 2(a)] and the experiment [Fig. 2(b)] revealed that plastic deformation is limited and concentrated near the fracture surface. From top to bottom, the regions are classified as bending, shearing, and tearing zones. The grain distortion in the metallographic image shows that the plastic zone is only about one-fourth of the material thickness. In contrast, a significantly larger region falls within the residual stress zone caused by elastic deformation. Since this elastic region cannot be directly observed on metallographic

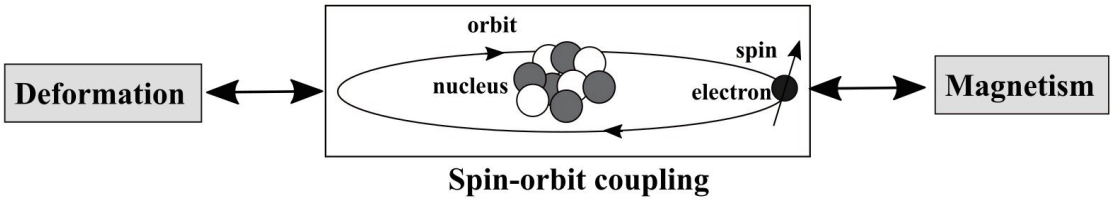

Fig. 1. Principle of magnetostriction and its effect on ES applications.

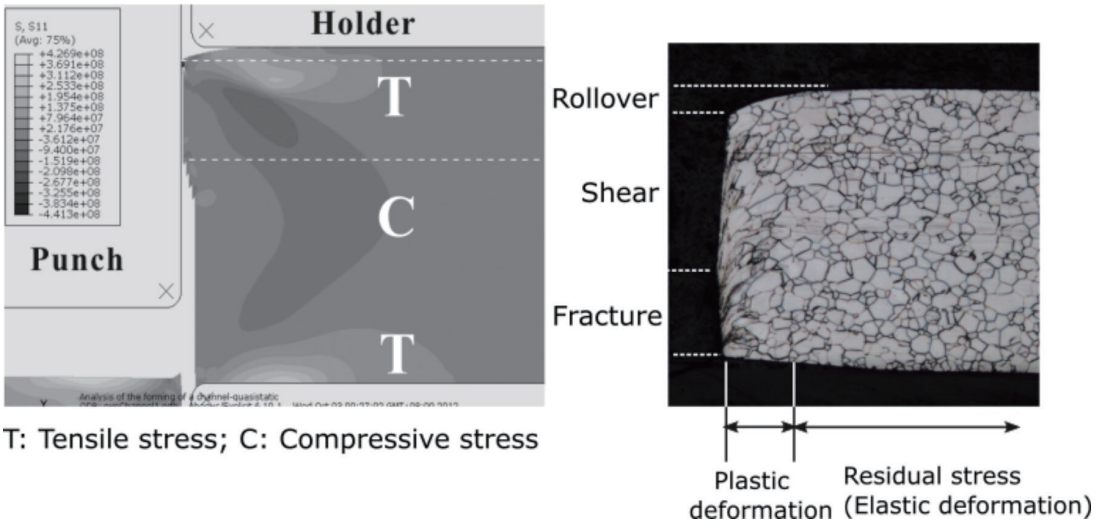

(a) (b)

Fig. 2. (a) Simulation result of punching process and (b) its crystallographic observation.

images, assessing its impact on magnetic degradation has long been a challenge. In our previous study, the needle-probe measurement techniques allowed us to estimate the range of this elastic region, which extends approximately four times the material thickness,[5] far exceeding the area of the plastic deformation zone. Therefore, compared with the more localized effects of plastic deformation, the inverse magnetostrictive effect induced by elastic deformation or residual stress plays a much more critical role in altering magnetic properties.

The aim of this study is to develop a benchtop measurement platform for ES to characterize inverse magnetostrictive properties using a single-sheet sample. In previous studies, a magnetic measurement setup was generally combined with a tensile testing machine, allowing observations under different stress and deformation conditions. Figure 3 shows a common setup, where electromagnetic steel sheets are stacked into a 20-mm-thick core, and magnetic flux is measured using coils.[6] Because of the large cross-sectional area of 400 mm^2, applying even a modest 30 MPa compressive stress requires an external force of 1200 kg, necessitating a specialized hydraulic press. The main drawbacks of such combined systems are their lack of integration, the need for significant external force, high setup costs, and large equipment. In this study, we develop a highly integrated measurement system based on the needle-probe technique and the theory of elasticity, enabling magnetic flux density (B)–magnetic field strength (H) loop measurements under both tensile and compressive elastic deformations using a single-sheet specimen. The proposed approach introduces several key features. First, the plane-stress elasticity principle is utilized to generate an equivalent compressive strain through Poisson's effect, allowing the compressive behavior to be evaluated without external compression loading. Second, a dual-core excitation structure is employed to ensure symmetric magnetic flux distribution across the sheet thickness. Third, the entire system is implemented as a compact and integrated testing platform capable of measuring magnetic properties under controlled elastic

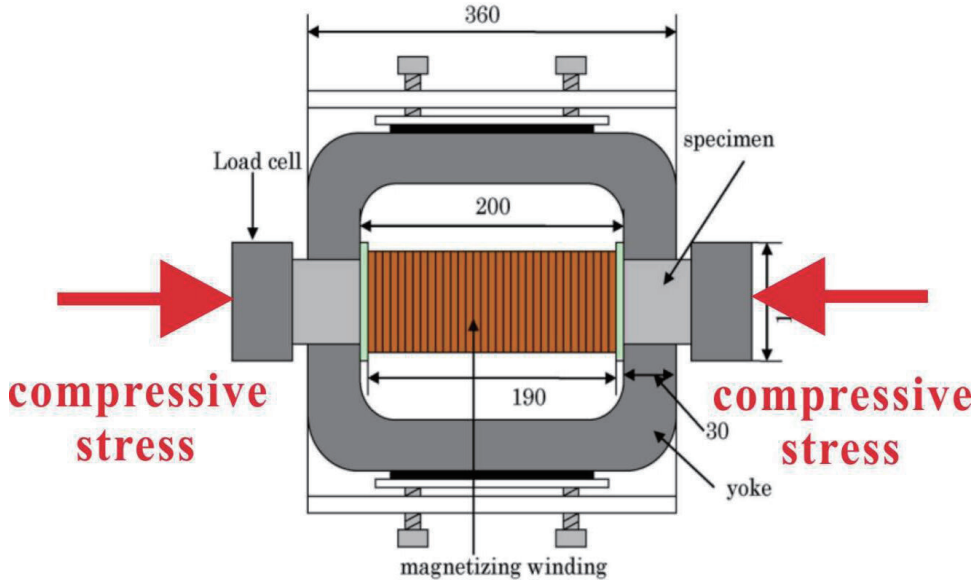

Fig. 3. (Color online) Common setup for generating compressive stress on magnetized steel sheets.[6]

deformation. In Sect. 2, we describe the measurement principles and system design used. The calibration procedure using standard-based correction factors is presented in Sect. 3. In Sect. 4, the inverse magnetostrictive measurement results for ES sheets with different iron-loss grades are reported, and Sect. 5 is a summary of the main findings of this study.

2. Measurement System Development

Our measurement system utilizes a needle-probe-based magnetic flux sensing method, achieving a compact size by eliminating the need for coil installation. Additionally, by incorporating the plane stress deformation principle, the detection of magnetic variations caused by compressive deformation is enhanced compared with previously developed systems.

2.1 Theory of elastic deformation

Since conventional tensile testing equipment is bulky and expensive, we use a single-sheet testing approach to reduce the required force by minimizing the laminated cross section. On the other hand, applying compression to a single-sheet material can easily cause buckling [Fig. 4(a)]. We address this issue by changing the magnetic field direction. As shown in Fig. 4(b), when the material is under tensile stress, the magnetization direction is aligned with the tensile force (x-direction), allowing the measurement of the tensile strain's effect on magnetism. To measure the effect of compressive strain, the needle probe and magnetization direction are simply rotated by 90 deg. Since metals follow elastic behavior within the yield strength, the deformation in the perpendicular (y-) direction represents the compressive strain given by

$$\varepsilon_y = -\nu\varepsilon_x, \tag{1}$$

where $\nu = 0.33$ is Poisson's ratio.[7] This approach enables compressive deformation without the need for additional applied pressure. The validity of the equivalent compressive strain is based on the plane-stress condition for thin sheets within the elastic regime. To further verify this assumption, a two-dimensional plane-stress FEM simulation was performed, as shown in Fig.

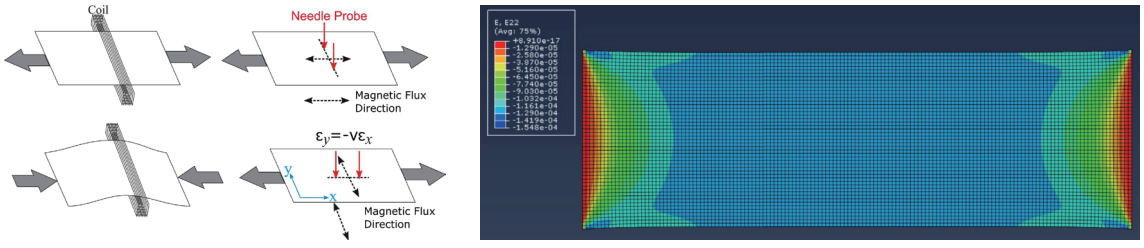

(a) (b)

Fig. 4. (Color online) Measurement principle of the device. (a) Buckling occurs after applying compressive force to a single sheet; right: use of needle probe to pick up magnetic flux in vertical direction. (b) FEM verification of equivalent compressive strain based on the plane-stress assumption.

4(b). The ES sheet model was subjected to a tensile strain of 400 με in the *x*-direction. Because of Poisson's effect, a transverse compressive strain of approximately 130 με was generated in the *y*-direction. The simulation results show that, except for regions close to the clamping boundaries, the transverse compressive strain remains nearly uniform across the central measurement area. This confirms that the Poisson-induced compressive strain provides a reasonable approximation for evaluating the inverse magnetostrictive behavior in the present setup.

2.2 *B*–*H* loop measurement

The needle-probe technique is a nondestructive method for measuring the magnetic flux inside an ES.[8] The measurement principle of the needle probe is similar to that of the searching coil, which all stem from the Maxwell–Faraday equation in its integral form as follows.

$$\int_C \bar{E} \cdot d\bar{l} = -\frac{\partial}{\partial t} \iint_A \bar{B} \cdot \hat{n} dA \tag{2}$$

Equation (2) explains that the magnetic flux through an area A can be estimated by measuring the induced voltage along its boundary C. Figure 5 further defines this contour precisely. The arrangement in Fig. 5(a) was specifically designed to measure the magnetic flux near the cutting edge, as contour C encloses the deformed area resulting from the cutting process.[3,5] In this study, the configuration in Fig. 5(b) is used since the area A represents the substrate without any induced stresses. The center segment 3→4 does not generate voltage because $\bar{E} = 0$ owing to the symmetry of the magnetic flux direction. Unlike the commonly used searching coil, the probe method requires neither drilling nor coil winding, making it more convenient to convert the magnetic flux into a measurable voltage signal. Given the probe signal's extremely low amplitude, an op-amp was used to boost it for digitization and subsequent numerical integration over time. The magnetic field strength H is measured using a magnetoresistive chip. Conventional needle-probe systems are typically used for local magnetic flux measurements under stress-free conditions.[3,5] In contrast, the proposed system integrates the plane-stress

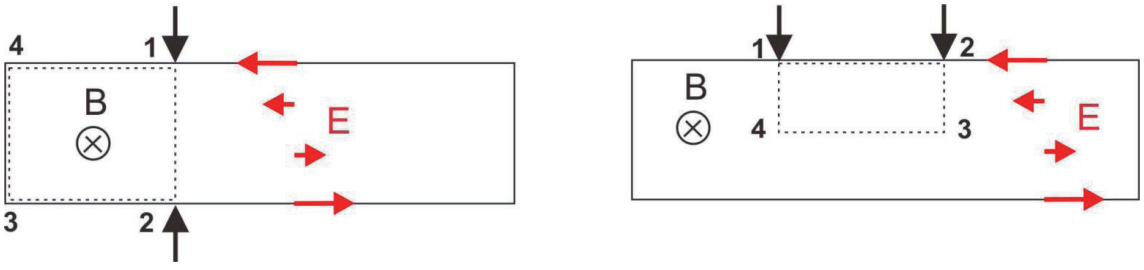

(a) (b)

Fig. 5. (Color online) Needle-probe measurement principle. Probe tips placed (a) on opposite surfaces and (b) on the same surface.

deformation principle to enable both tensile and equivalent compressive magnetic characterizations using a single-sheet specimen without requiring external compressive loading equipment.

To achieve uniformity in flux distribution within the cross section of the test sample, we also examine the differences between single-core and dual-core excitations in magnetic circuit design. As shown in Fig. 6(a), the single core excites only the upper surface, while the dual core excites both surfaces simultaneously. First, finite element simulation is carried out to analyze the magnetic field distribution. The results show that single-sided excitation has an uneven flux density distribution in the thickness direction [Fig. 6(b)]. When excitation is applied only to the top surface, the flux density difference between the top and bottom surfaces becomes 1.5 times. This means that the magnetic flux seeks a path of low reluctance, and hence, alters the symmetry of the flux distribution, rendering the integration path in Fig. 5(b) invalid. In contrast, the double-sided excitation method produces a more uniform and symmetric magnetic flux density in the single-sheet sample, as clearly shown in Fig. 6(b). It also highlights the skin effect, where the magnetic flux density is higher near the surface. The measured *B*–*H* loops for the two excitation methods are shown in Fig. 7. The *B*–*H* loop obtained with a single core is highly affected by the sample width [Fig. 7(a)]. In contrast, the dual-core measurement in Fig. 7(b) shows consistent results. Even with a 4× difference in specimen width (60 mm/15 mm), the *B*–*H* loops remain highly overlapping.

2.3 System integration

Using the aforementioned design concepts, a highly integrated measurement system can be developed, as shown in Fig. 8. A single-sheet sample is placed in the mechanism, where a tensile structure induces deformation. The measurement platform, equipped with a load cell, applies up to 90 MPa of tensile stress, inducing a perpendicular compressive deformation of 30 MPa owing

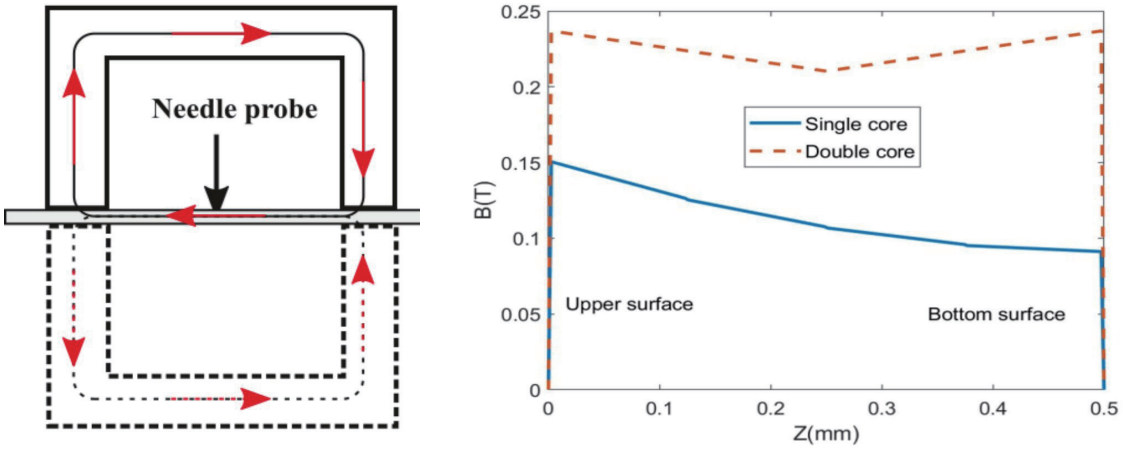

(a) (b)

Fig. 6. (Color online) Advantages of dual-core excitation. (a) Single- and double-core excitations. (b) Simulation results of magnetic flux density.

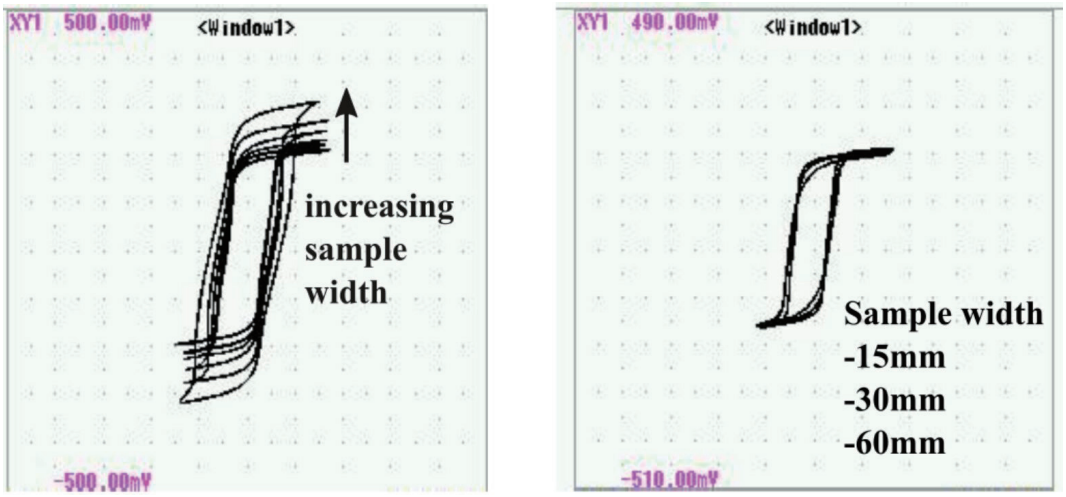

(a) (b)

Fig. 7. (Color online) *B–H* loop measurement results. (a) Effect of test specimen width on single core. (b) Consistent excitation effect achieved with dual core.

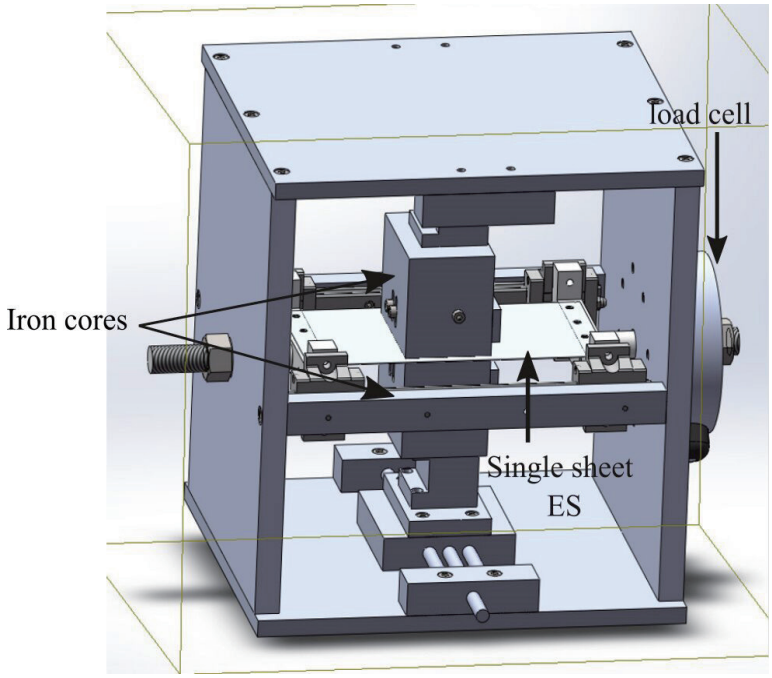

Fig. 8. (Color online) Measurement platform design.

to Poisson's effect. Furthermore, the iron cores can rotate 90 degrees to facilitate measurements in the compressive direction. To enable real-time measurement, a LabVIEW-based data processing program was developed to numerically integrate the time-varying flux signal from the probe after 100-fold analog amplification, obtaining the magnetic flux ϕ. Figure 9 shows the user interface, displaying the real-time *B–H* loop during testing.

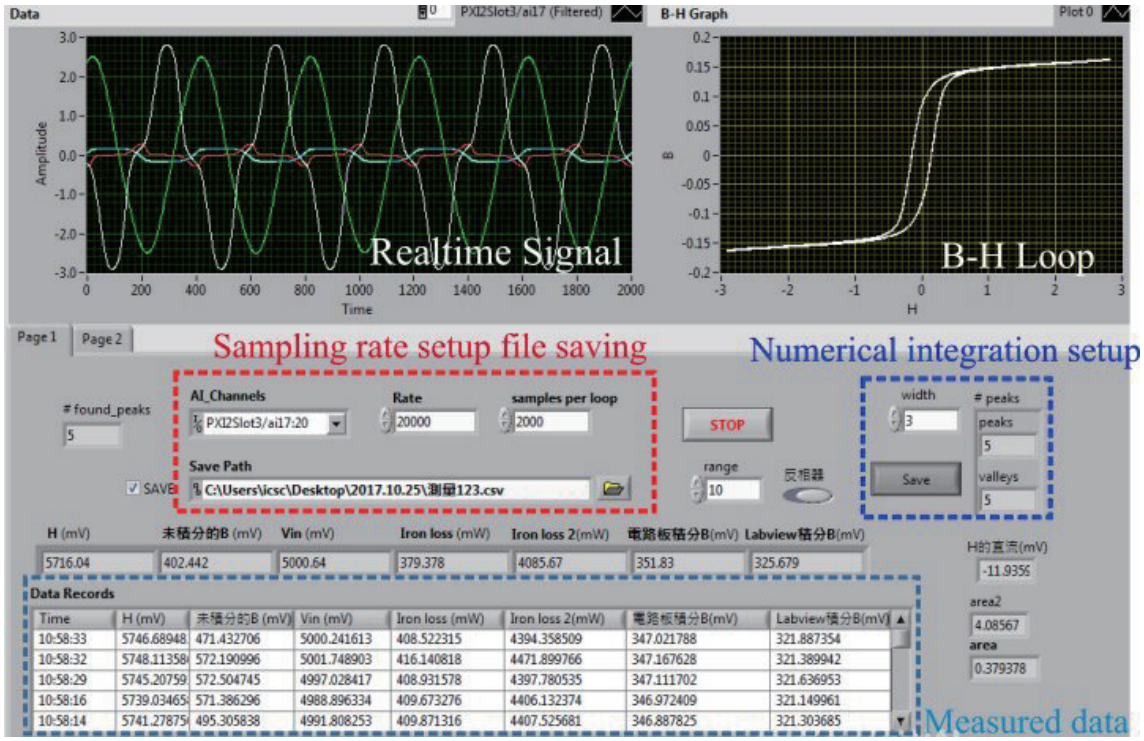

Fig. 9. (Color online) User interface for operation and display.

3. System Calibration

Calibration is required to convert the measured voltage signals corresponding to B and H into standard physical units (tesla and A/m). In this study, the calibration procedure is established using the reference magnetic data obtained from the Epstein frame measurement in accordance with ASTM A1306-04. The calibration process consists of two steps: (1) the reconstruction of an equivalent *B*–*H* curve using measurements along two orthogonal directions and (2) the determination of calibration coefficients using reference Epstein data.

3.1 Reconstruction of the equivalent *B*–*H* curve

Although ES used in motor laminations is generally classified as non–grain-oriented (NO), practical materials still exhibit slight magnetic anisotropy owing to manufacturing processes such as rolling and annealing. Consequently, the magnetic properties measured along the rolling and transverse directions are not identical. In a conventional Epstein frame setup (Fig. 10), sheet samples cut along both rolling and transverse directions are arranged alternately to form a magnetically closed loop. During excitation, the magnetic flux passes through both types of specimens, so that they experience the same magnetic flux density ($B = B_{//} = B_{\perp}$), while the magnetizing field strengths required in the two directions differ. According to Ampere's law,

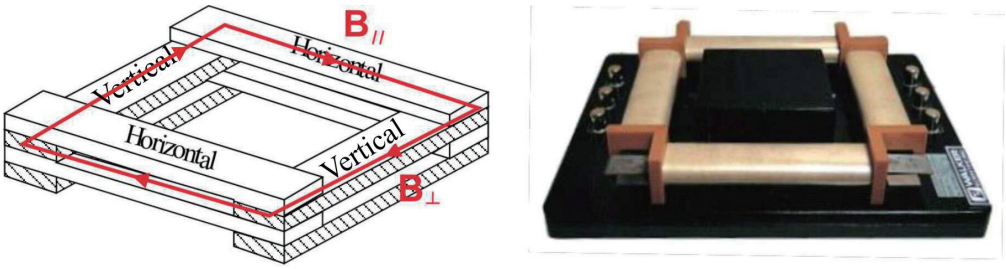

Fig. 10. (Color online) Epstein frame formed by a magnetically closed magnetic path using rolling and transverse samples.

$$\oint_C \bar{H} \cdot d\bar{l} = H_{//} \frac{L}{4} \times 2 + H_{\perp} \frac{L}{4} \times 2 = \frac{H_{//} + H_{\perp}}{2} L, \tag{3}$$

where L represents the total magnetic path length of the Epstein loop, while $H_{//}$ and $H_{\perp}$ denote the magnetizing field strengths in the rolling and transverse directions, respectively. The equivalent magnetic field strength H_{eq} obtained from the Epstein configuration can therefore be expressed as

$$H_{eq} = \frac{H_{//} + H_{\perp}}{2}. \tag{4}$$

In the proposed system, the needle probe can be rotated by 90°, enabling the measurement of the B–H curves along both the rolling and transverse directions of the sheet. As shown in Fig. 11, the rolling direction exhibits a slightly higher magnetic performance than the transverse direction, which is consistent with typical characteristics of ES. The equivalent B–H curve is reconstructed by averaging the magnetic field strengths corresponding to the same flux density.

3.2 Determination of calibration coefficients

In the present system, both magnetic flux density and magnetic field strength are obtained from the measured voltage signals. Therefore, calibration coefficients are required to convert these signals into physical quantities. Following ASTM A1306-04,[9] the relationship between the Epstein reference measurement and the present single sheet tester (SST)-type measurement can be expressed using the calibration coefficients C_H and C_B. For magnetic field strength,

$$H_p = C_H H_a, \tag{5}$$

where H_p is the magnetic field strength obtained from the Epstein measurement and H_a is the corresponding value measured by the proposed system. Similarly, the magnetic flux density can be expressed as $B_p = C_B B_a$, where B_p and B_a represent the flux densities obtained from the

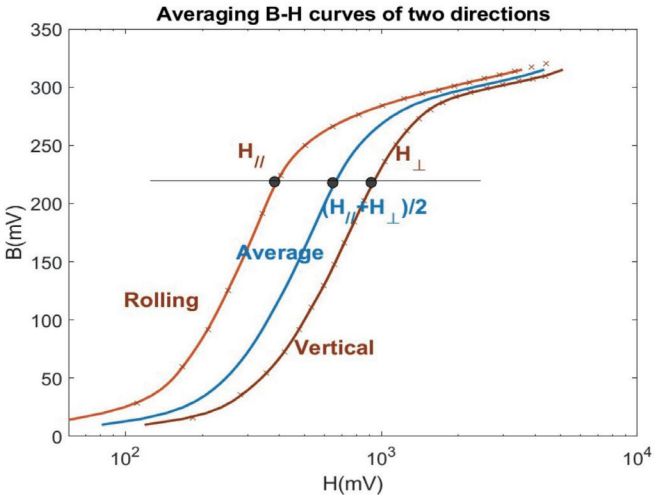

Fig. 11. (Color online) Reconstruction of the equivalent *B–H* curve by averaging the magnetic field strengths at identical flux density.

Epstein measurement and the present measurement system, respectively. The calibration coefficients are determined by comparing the measured *B–H* curve with the reference Epstein data. Both curves are plotted on a logarithmic scale, and the horizontal and vertical shifts required to align the knee point of the curves are used to determine the coefficients C_H and C_B. The knee region is selected because it represents a stable characteristic point of the magnetization curve and is less sensitive to measurement noise than the low-field region. As shown in Fig. 12, for the 0.5-mm-thick medium-loss (ML) ES sheet, the optimal alignment is obtained with calibration coefficients $(C_H, C_B) = (10^{-0.7}, 10^{-2.31})$. After applying these calibration factors, the calibrated *B–H* curve is in excellent agreement with the Epstein reference measurement, as illustrated in Fig. 13.

The repeatability of the measurement system mainly depends on the signal-to-noise ratio (SNR) of the detected probe voltage. Repeated measurements under identical experimental conditions revealed that the variation in measured magnetic flux density was approximately ±2–3% in the low-flux region. This variation decreases significantly near the knee point of the *B–H* curve, where the signal amplitude becomes larger relative to the noise level. These results indicate that the proposed measurement system provides good repeatability and stability.

4. Measurement Results

After the development of our equipment was completed, initial testing was conducted using commercially available materials. For the motor design community, one of the most challenging issues is the discrepancy between the design and actual characteristics caused by stress and deformation during manufacturing. To address this, we measured three representative materials to provide reference data on the degradation of magnetic properties for motor design. The selected materials, ranked by increasing iron loss, are designated as SL (small loss), ML (medium loss), and LL (large loss). The following measurements were conducted with 50 Hz

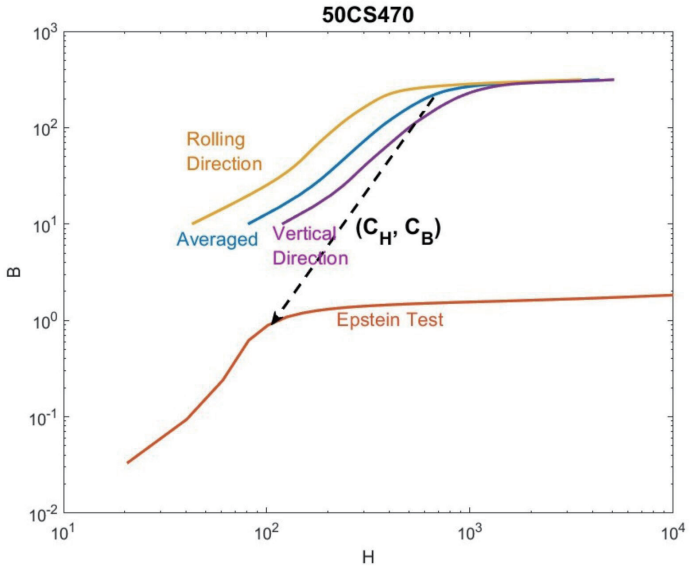

Fig. 12. (Color online) Determination of calibration coefficients CH and CB by aligning knee points of logarithmic *B–H* curves.

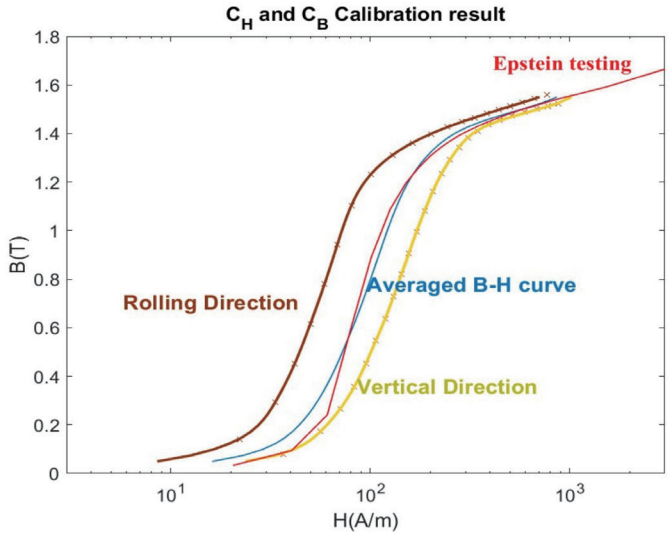

Fig. 13. (Color online) Calibrated *B–H* curve and Epstein reference measurement.

excitation, and the obtained the *B–H* curves are presented on a linear scale to better observe their variations. Figures 14 and 15 respectively show the changes in the *B–H* curves of SL after undergoing different levels of tensile and compressive deformations. It can be observed that both tensile and compressive deformations have negative impacts on the magnetic properties of the material, with compressive deformation causing a more severe impact.

The impact on the knee point is obvious, as demonstrated by notable differences between the curves. However, as saturation is approached, these curves tend to converge, indicating that the

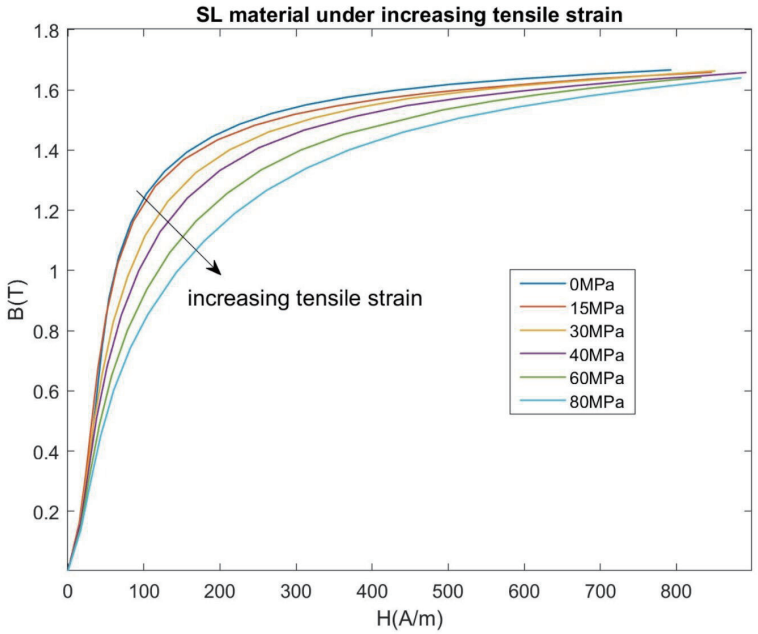

Fig. 14. (Color online) *B*–*H* curves of SL samples under tensile deformation.

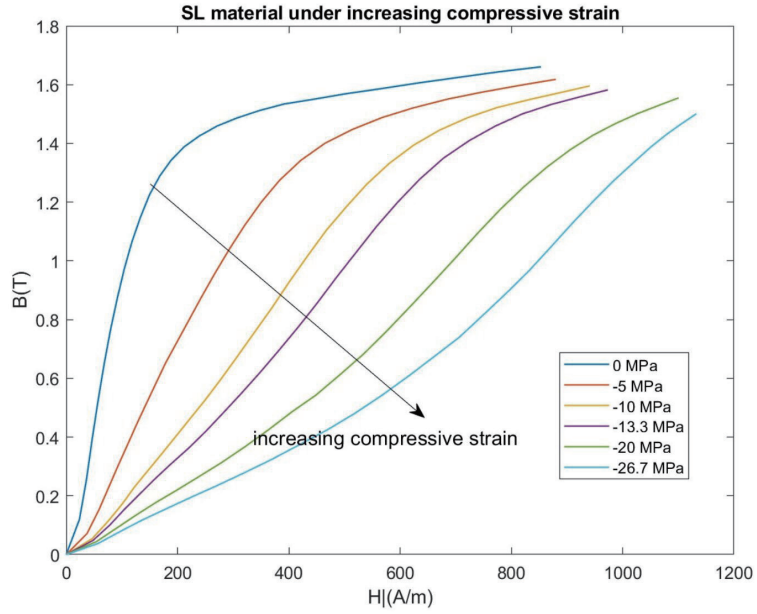

Fig. 15. (Color online) *B*–*H* curves of SL samples under compressive deformation.

effect of stress on the saturation magnetic flux density diminishes, which is consistent with the phenomena recorded in the literature.[10] The results show that elastic deformation, especially compressive stress, significantly affects permeability in the initial linear range of the *B*–*H* curve, with changes up to several times. Figures 16 and 17 depict magnetic changes from ML samples with tensile and compressive deformations. Similar to SL, but in compressive

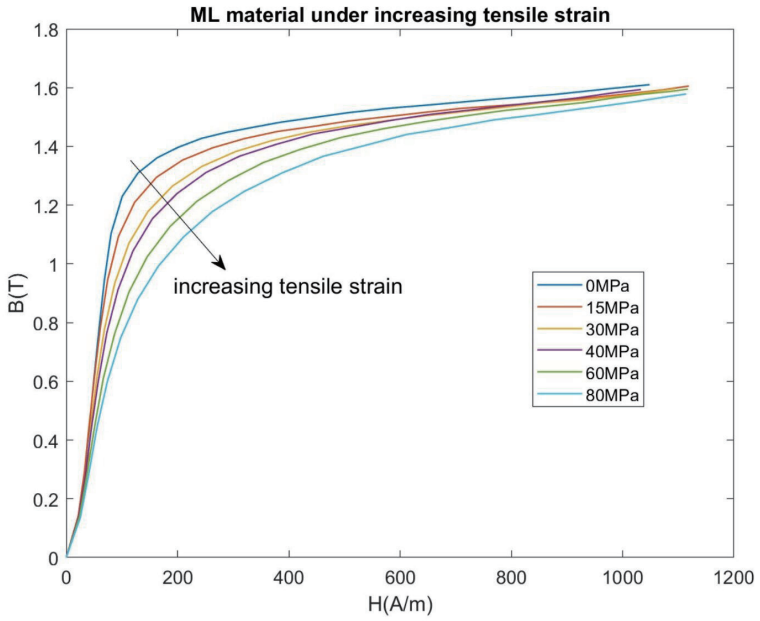

Fig. 16. (Color online) *B–H* curves of ML samples under tensile deformation.

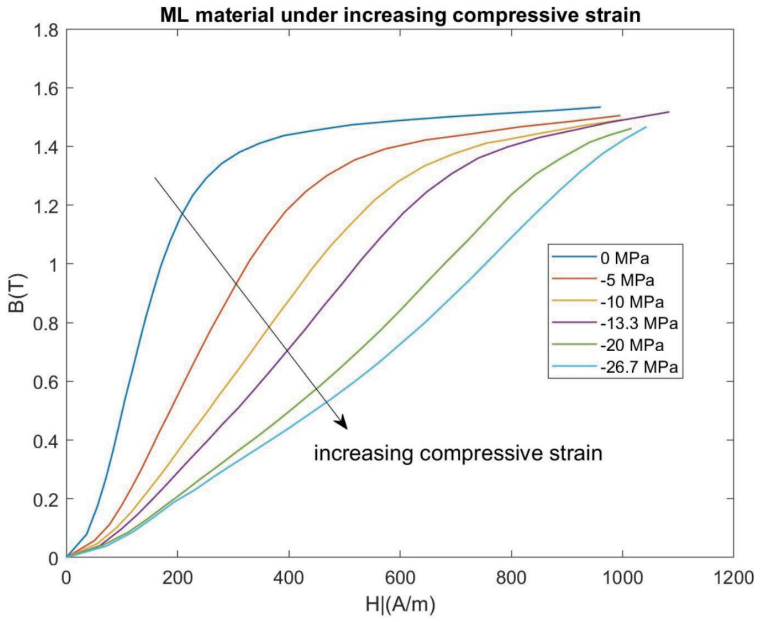

Fig. 17. (Color online) *B–H* curves of ML samples under compressive deformation.

deformation, the magnetic degradation is slightly reduced, with permeability in the low-flux-density range being slightly higher than that in SL samples.

Finally, Fig. 18 shows the LL sample's changes under tensile deformation. Unlike the degradation in the other two materials, the permeability slightly increases at low stress, dropping

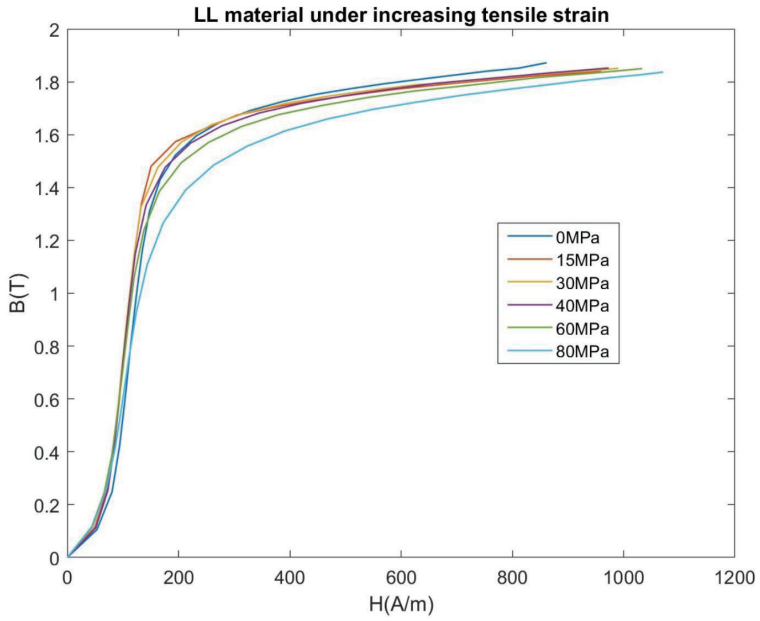

Fig. 18. (Color online) *B*–*H* curves of LL samples under tensile deformation.

only above 40 MPa, suggesting that tensile deformation enhances magnetic flux within a certain range. Conversely, compressive deformation has a negative effect, though it is notably weaker than that in the case of SL (Fig. 19). These findings are insightful: despite higher iron loss and lower permeability, LL materials exhibit the highest resistance to deformation-induced magnetic degradation.

Since compressive strain affects ES much more than tensile strain, we compare the *B*–*H* curves of three materials at maximum compression to highlight its impact on magnetism. Figure 20 shows the differences in materials under zero stress (solid line) and 27 MPa compression (dashed line). It is evident that SL samples exhibit the greatest difference after compression, indicating the most severe permeability degradation, followed by ML samples, while LL materials are the least affected.

Beyond investigating material properties, these measurement results can also serve as a reference for future motor performance evaluations. In certain applications, maintaining a constant output torque is essential.[11] Since torque depends on flux density, increasing the excitation current to compensate for the decay caused by compressive stress during assembly or manufacturing can lead to a significant rise in copper loss. This effect is illustrated in Fig. 21. When the electromagnetic steel sheet undergoes deformation, its *B*–*H* curve shifts to the right. Maintaining the same flux density B requires a higher magnetizing intensity H. Motor designs typically rely on Epstein's stress-free testing data to achieve the rated torque at B = 1.4 T with H_0. However, material degradation increases the required magnetizing intensity to H_σ, resulting in an excitation current ratio of H_σ/H_0. Since copper loss is proportional to the square of this ratio $[(H_\sigma/H_0)^2]$, the increase in loss becomes substantial.

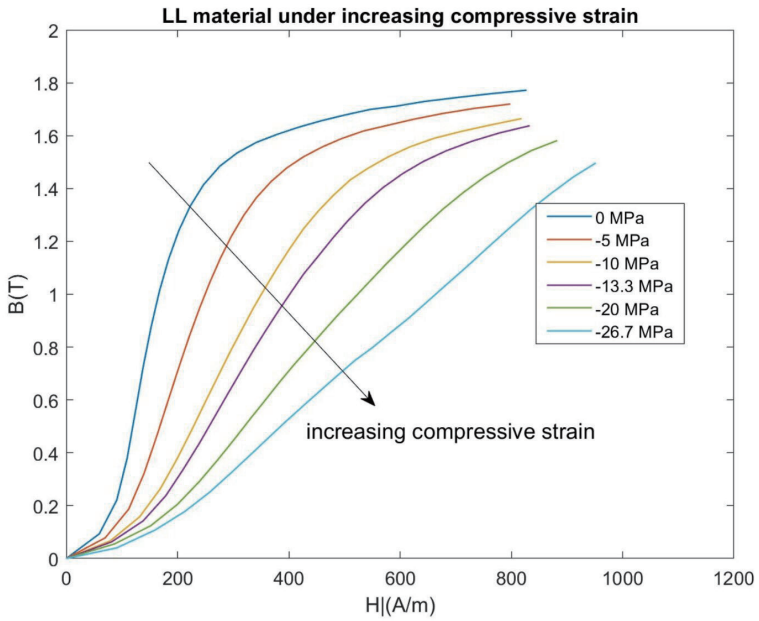

Fig. 19. (Color online) *B*–*H* curves of LL samples under compressive deformation.

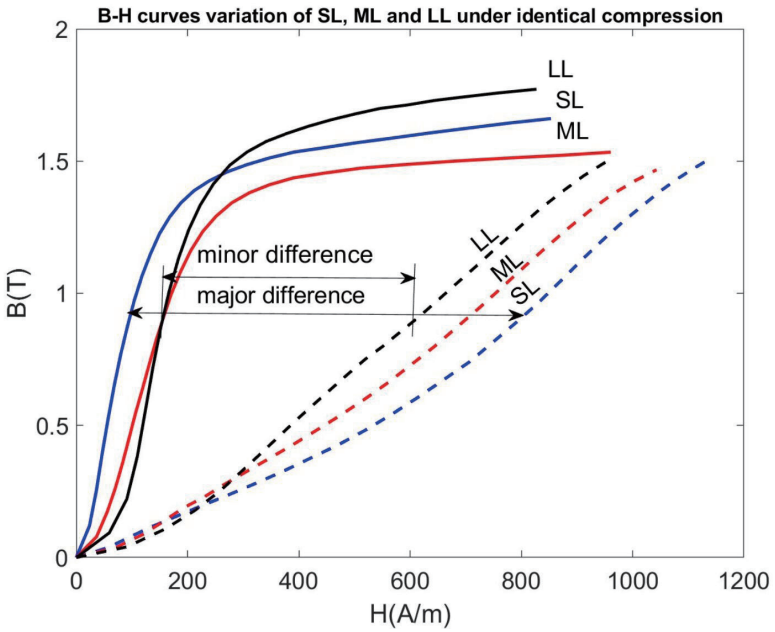

Fig. 20. (Color online) *B*–*H* curves of three types of material under zero stress (solid line) and 27 MPa compression (dashed line).

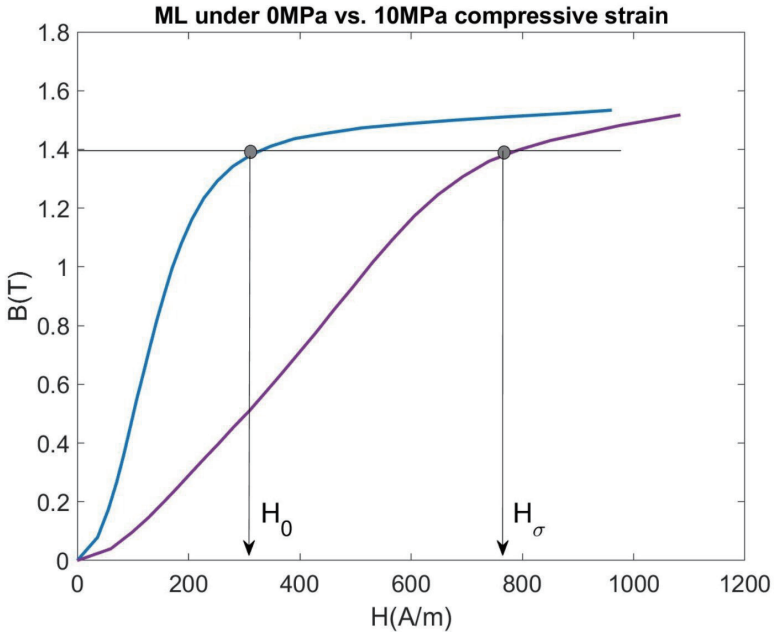

Fig. 21. (Color online) Copper loss is expected to increase markedly owing to compressive deformation.

5. Conclusions

In this study, we employed needle-probe techniques and principles of elasticity to develop an innovative device for measuring the magnetic property variations of ES under both tensile and compressive deformations. The device is highly integrated, compact, and easy to operate, providing Epstein frame-consistent results when unloaded. It was first applied to measuring 0.5-mm-series ES sheets, marking the first systematic comparison of three benchmark products with different iron loss specifications. Two significant observations were obtained from measurement results. First, the magnetic degradation caused by compressive deformation is much higher than that caused by tensile deformation. Second, high-iron-loss materials exhibit a greater resistance to magnetic degradation under compressive deformation than low-iron-loss materials. These measurement results can serve as a reference for motor manufacturers and material developers.

Acknowledgments

This work was partially supported by the National Science and Technology Council (NSTC) of Taiwan under Grant No. NSTC-114-2222-E-992-008-MY2. The authors declare that they have no conflict of interest.

References

1 B. D. Cullity and C. D. Graham: Introduction to Magnetic Materials, (John Wiley & Sons, Hoboken, 2008) 2nd ed., Chap. 8.4, pp. 257–258. https://doi.org/10.1002/9780470386323
2 Z. Gmyrek: Electr. Rev. (2012) 263. https://doi.org/10.1109/ICEMS.2014.7014017
3 S.-K. Kuo, W.-C. Lee, S.-Y. Lin, and C.-Y. Lu: IEEE Trans. Ind. Appl. **51** (2015) 4357. https://doi.org/10.1109/ICEMS.2014.7014017
4 A. Selema, M. Ibrahim, and P. Sergeant: Energies **15** (2022) 17862. https://doi.org/10.3390/en15217862
5 S.-K. Kuo, W.-C. Lee, and S.-Y. Lin: Proc. 34th Symp. Electr. Power Eng. (Taichung, Taiwan, 2013) 3041–3046. https://shorturl.at/JvFfR
6 D. Miyagi, K. Miki, M. Nakano, and N. Takahashi: IEEE Trans. Magn. **46** (2010) 318. https://doi.org/10.1109/TMAG.2009.2033550
7 F. P. Beer: Mechanics of Materials (McGraw-Hill Higher Education, New York, 2009) Chap. 2.11, pp. 93–94.
8 M. D. Wulf, L. Dupre, D. Makaveev, and J. Melkebeek: J. Appl. Phys. **93** (2003) 8271. https://doi.org/10.1063/1.1544485
9 ASTM Standard A1306-04: Standard Guide for Measuring Power Frequency Magnetic Properties of Flat-Rolled Electrical Steels Using Small Single Sheet Testers. https://doi.org/10.1520/A1036-04R20
10 L. Li: Stress Effects on Ferromagnetic Materials: Investigation of Stainless Steel and Nickel (Ph.D. Dissertation, Iowa State University, 2004). https://doi.org/10.31274/rtd-180813-8795
11 P. Krause, O. Wasynczuk, S. Sudhoff, and S. Pekarek: Analysis of Electric Machinery and Drive Systems, (IEEE Wiley Press, Hoboken, 2013) 3rd ed. https://doi.org/10.1002/9781118524336

About the Authors

Guan-Ming Chen received his B.S. degree in mechanical engineering from National Cheng Kung University, Tainan, Taiwan, in 2004. He received his M.S. and Ph.D. degrees in electrical engineering from National Sun Yat-sen University, Kaohsiung, Taiwan, in 2006 and 2013, respectively. From 2013 to 2015, he was a senior engineer at Sunonwealth Electric Machine Industry Co., Ltd., where he focused on motor design. Since 2015, he has been a research scientist with China Steel Corporation, Kaohsiung, Taiwan, specializing in the application research of electrical steel sheets. His research interests include motor design, the development of high-efficiency motors for drones and electric vehicles (EVs), the design of thermoelectric elements, and semiconductor process integration. He is also an expert in motor electromagnetic simulation and material analysis for electrical steel. (189837@mail.csc.com.tw)

Wei-Hao Chang received his Ph.D. degree in electrical engineering from National Taiwan University, Taipei, Taiwan, in 2009. His doctoral research focused on portable magnetic resonance technology. He is currently a research scientist working on the nondestructive testing (NDT) of steel products in the Green Energy & System Integration R&D Department at China Steel Corporation, Kaohsiung, Taiwan.

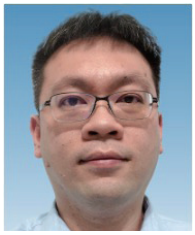

Kai-Fan Lo received his B.S. and M.S. degrees in mechanical engineering from Yuan Ze University, Taoyuan, Taiwan, in 2004 and 2006, respectively, and his Ph.D. degree in power mechanical engineering from the National Tsing Hua University, Hsinchu, Taiwan, in 2012. From 2012 to 2014, he was a researcher with the Industrial Technology Research Institute (ITRI), Taiwan. Since 2015, he has been a researcher with China Steel Corporation (CSC), Kaohsiung, Taiwan. His research interests include industrial data analytics, applied artificial intelligence, and fuel cell design. (189795@mail.csc.com.tw)

Shih-Kang Kuo received his B.S. and M.S. degrees in power mechanical engineering from the National Tsing Hua University, Hsinchu, Taiwan, in 1996 and 1998, respectively, and his Ph.D. degree in mechanical engineering from The Ohio State University, Columbus, in 2003. From 2005 to 2024, he was a research scientist with China Steel Corporation, Kaohsiung, Taiwan. He is currently an assistant professor at the Department of Mechanical Engineering, National Kaohsiung University of Science and Technology (NKUST), Kaohsiung, Taiwan. His research interests include magnetic measurement technologies and measurement and analysis techniques for residual stress. (kuo67@nkust.edu.tw)